A Digital Pediatric Brain Structure Atlas from T1-Weighted MR Images

Zuyao Y. Shan[1], Carlos Parra[2], Qing Ji[1], Robert J. Ogg[1], Yong Zhang[1],
Fred H. Laningham[3], and Wilburn E. Reddick[1,2]

[1] Division of Translational Imaging Research, Department of Radiological Sciences,
St. Jude Children's Research Hospital, Memphis, Tennessee 38105, USA
[2] Department of Biomedical Engineering, The University of Memphis,
Memphis, TN 38152, USA
[3] Division of Diagnostic Imaging, Department of Radiological Sciences,
St. Jude Children's Research Hospital, Memphis, Tennessee 38105
zuyao.shan@stjude.org

Abstract. Human brain atlases are indispensable tools in model-based segmentation and quantitative analysis of brain structures. However, adult brain atlases do not adequately represent the normal maturational patterns of the pediatric brain, and the use of an adult model in pediatric studies may introduce substantial bias. Therefore, we proposed to develop a digital atlas of the pediatric human brain in this study. The atlas was constructed from T1-weighted MR data set of a 9-year old, right-handed girl. Furthermore, we extracted and simplified boundary surfaces of 25 manually defined brain structures (cortical and subcortical) based on surface curvature. We constructed a 3D triangular mesh model for each structure by triangulation of the structure's reference points. Kappa statistics (cortical, 0.97; subcortical, 0.91) indicated substantial similarities between the mesh-defined and the original volumes. Our brain atlas and structural mesh models (www.stjude.org/brainatlas) can be used to plan treatment, to conduct knowledge and model-driven segmentation, and to analyze the shapes of brain structures in pediatric patients.

1   Introduction

Atlases based on MR images provide more useful information than do anatomy books in activities such as the planning of neurosurgical interventions, because the medical team can visualize the brain three-dimensionally, because data are available electronically, and because anatomic shape is based on in vivo images rather than fixed-brain slices [1]. Several atlases of human brain structures based on MR images have been developed for different applications, for example, an early digital three-dimensional brain atlas that was commercially available for the teaching of neuroanatomy [2]. Because this atlas was intended primarily for teaching, it was relatively difficult to use interactively, and the data set from which the atlas was constructed was not accessible for further development. Furthermore, the images that were used had been derived from a patient with localized pathology [3]. Also available commercially was a computerized brain atlas developed specifically for

brain mapping [4]. For use in surgical planning, researchers at the Surgical Planning Laboratory at Brigham and Women's Hospital (Boston) developed a web-interactive and highly detailed brain atlas, which was very good for visualizing brain structures (splweb.bwh.harvard.edu).

One of the most prominent examples of brain atlases would be the one that will be constructed by the International Consortium for Brain Mapping (ICBM). In the final product of this project, a human brain atlas will be constructed from MR images, CT data, and post-mortem frozen sections sliced with giant cryomicrotoms. Although the labor-intensive labeling is not finished yet, the consortium has provided an anatomic template based on the MR images of a single subject (www.loni.ucla.edu/ICBM). Due to the limited length of paper, other brain atlases, including atlas based on single-subject brain from Montreal Neurological Institute (MNI) [5], were not reviewed here.

Many atlases have been developed for different applications; however, to the best of our knowledge, no digital atlas of pediatric brain structures has been available until now. A pediatric atlas is needed because the human brain continues to develop throughout childhood and adolescence [6] and the use of an adult template in pediatric neuroimaging studies may introduce significant bias [7]. Kates et al. [8] revised the original Talairach atlas grid to increase its applicability to pediatric brains. Revising the sectors to fit the brains of children resulted in the same or better accuracy, i.e. the sensitivity for lobes improved to 0.79~0.95 compared with manual tracing. However, for small structures such as brain stem, the mean volume difference between automatic and manual results was 59.4%. A possible reason could be due to the fact that the accuracy of Talairach system has been limited by its fixed grid numbers. Therefore, studies described above such as ICBM have been performed to construct adult brain atlas other than the Talairach system. Similarly, we proposed to develop a pediatric brain atlas in this study.

2   Materials and Method

2.1   MR Image

A three-dimensional T1-weighted MR image of a Caucasian, 9-year old, right-handed girl was used in this study. The weight and height of the girl were 27.27 Kg and 132 cm that place her at the 50 and 40 percentile for height and weight in healthy children population, respectively (www.cdc.gov/growthcharts). The girl had no history of psychiatric, neurological, or learning problems. The MR imaging had been conducted under an approved protocol and with written informed consent from the patient, parent, or guardian, in accordance with guidelines of the St. Jude Children's Research Hospital Institutional Review Board, the National Cancer Institute, and the Office for Human Research Protection. Retrospectively using the MR data for our study has been approved by our Institutional Review Board.

The MR data were acquired by using a 1.5-T Symphony (Siemens Medical System, Iselin, NJ) whole-body imager with the standard circular polarized volume head coil. A three-dimensional MPRAGE T1-weighted sequence was used. Sagittal images were acquired by using the following imaging parameters: TR = 1800 ms, TE = 2.74 ms, flip angle = 15°, FOV = 210 mm×210 mm, number of slices (contiguous) = 128, slice thickness = 1.25 mm, and matrix = 512×512.

We spatially aligned the MR images to a pediatric template by using an affine registration algorithm. The registration algorithm was adopted from the affine registration method provided by SPM2 that is freely available on the web (www.fil.ion.ucl.ac.uk/spm). The object function used was normalized mutual information [9] and was maximized using Powell's golden search algorithm [10]. The pediatric brain template was available from Cincinnati Children's Hospital Medical Center (www.irc.cchmc.org) [7]. Templates are available for three age groups: young children (aged 5-9.5 years old), older children (aged 9.6-12.9 years old), and adolescents (aged 13-18.8 years). We used the pediatric template of young children. Finally, we resampled the MR images into isotropic voxels of 1 mm×1 mm×1 mm by using a trilinear algorithm.

2.2   Brain Structure Delineation

Brain structures were manually delineated by an experienced investigator with the help of anatomic books [11], previous reports [12, 13] and web-based interactive atlases of adult brains (www9.biostr.washington.edu/da.html and splweb.bwh. harvard.edu). The custom in-house software package used to delineate the structures allowed us to draw structures on sagittal and transverse slices and to view them in three orthogonal slices simultaneously. All 25 brain structures were then reviewed by an experienced radiologist for accuracy, and modified where necessary.

Left and right hemispheres were divided by the longitudinal fissure. Boundaries for subcortical structures were identical to those described in the references. However, white matter (WM) was included in the lobe segmentation, resulting in boundaries that differ slightly from those previously reported. Our rationale for including the WM in lobe segmentation is addressed in the Discussion.

Frontal Lobe. The boundaries for the frontal lobe were defined as follows. The lateral and anterior boundaries were defined by the natural limits on every image section. On sections of the superior surface where the central sulcus intersects the longitudinal fissure, the posterior boundary was set at the central sulcus. The inner boundary was defined by the longitudinal fissure (Fig. 1a). On sections that are inferior to the ones listed above, but superior to the sections containing ventricles, the posterior boundary were central sulcus and a vertical imaginary plane that connected the end of central sulcus and the longitudinal fissure or cingulate cortex. The inner boundary was defined as the longitudinal fissure or cingulate cortex (Fig. 1b). On sections that are inferior to the ones listed above, but superior to the sections containing insula, boundaries were similar to those in the previous sections except where the corpus callosum or ventricle starts. In these sections, the inner boundary was defined by the longitudinal fissure, cingulate cortex, corpus callosum, and ventricle (Fig. 1c). On sections containing the insula, the inner and posterior boundaries were defined by the insula, an imaginary plane that connected the anterior tip of the insula and the posterior tip of the corpus callosum, the cingulate cortex, and the longitudinal fissure (Fig1. d-g).

Parietal Lobe. The parietal lobe (PL) was defined by using the following boundaries: The anterior boundary was defined by the central sulcus and an imaginary plane that dropped vertically from the end of the central sulcus (Fig. 1b, c, and d). The superior
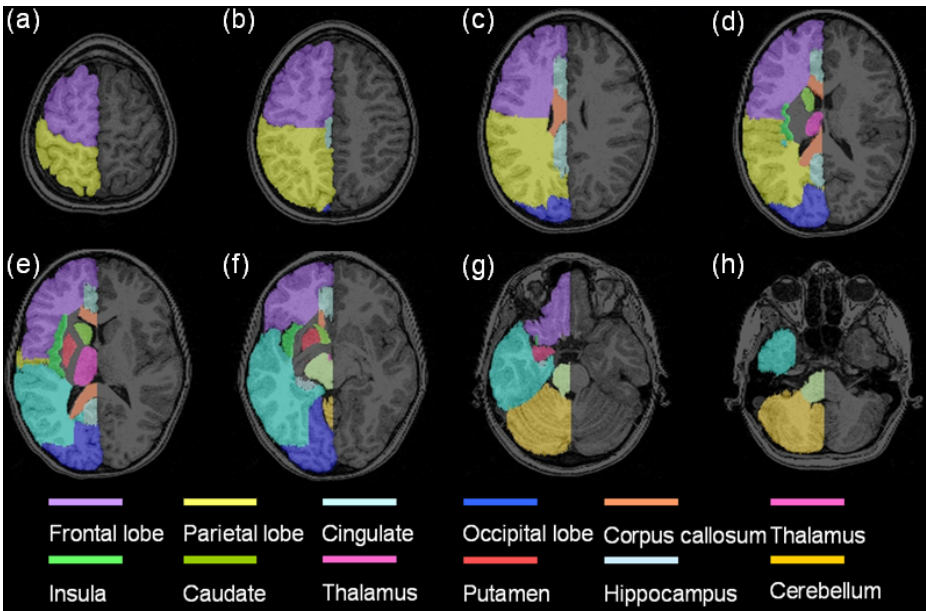
Fig. 1. Manual delineation of brain structures. The manually defined volumes of interest are illustrated on selected transverse slices. The representative slices are selected from 256 continuous slices, and the structures on the left hemisphere were selected for illustration purpose.

boundary was defined by the natural limit on every image section. The inferior boundary was defined by the lateral sulcus and an imaginary plane that extended horizontally from the point where the lateral sulcus changes from a horizontal to a vertical orientation (Fig. 1e). The posterior boundary was defined by the parietal-occipital sulcus (Fig 1. b and c) and an imaginary plane that projected from the superior tip of the parietal-occipital sulcus to the preoccipital notch on image sections where the parietal-occipital sulcus disappears (Fig. 1. d-f). Because the preoccipital notch was very difficult to identify on the MR image, we used the posterior tip of the inferior temporal gyrus as an approximation of its location. The inner boundary of the PL was defined by the longitudinal fissure (Fig. 1a), cingulate cortex (Fig. 1b), ventricle and corpus callosum (Fig. 1c), and the insula and an imaginary plane that projected from the posterior tip of the insula to the ventricle (Fig. 1d).

Temporal Lobe. The temporal lobe was defined by using the following boundaries. The superior and posterior boundaries were defined by the inferior boundary of the PL described above. The inner boundary was defined by the insula, an imaginary plane that projected from the posterior tip of the insula to the ventricle (Fig. 1e), the ventricle, the corpus callosum, and the hippocampus. The inferior boundary was defined by the natural limit within each imaging section.

Occipital Lobe. The occipital lobe was defined by using the following boundaries. The anterior boundary was defined by the posterior boundary of the PL described

above. The superior, posterior, and inferior boundaries were defined by the natural limit within each imaging section.

2.3 Triangular Mesh Models

The manually defined structures were further developed into individual triangulated mesh models. The boundaries of structures were extracted by using a 26-member neighborhood. The boundaries were then simplified on the basis of the surface curvature. The boundaries for each structure were scanned in order (X, Y, and Z coordinates). The first voxel encountered was defined as the vertex of the boundaries and as the first focal point. For each focal point (s), the other boundary points (N = N − {s}, N is the set of all boundary points) were first divided into groups of neighborhoods with different radiuses (r_i) defined by the surface distance from points to the focal point. Then, beginning with the group that has the smallest radius, if the normal angle of the group with a radius of r_i (N_g) was smaller than the threshold angle, all points in this group were removed (boundary points N were updated here, N $= N - N_g$) and the group with a radius of r_{i+1} was evaluated. If the normal angle of the group was equal to or larger than threshold angle, the point with the smallest X, Y, and Z coordinates in this group was selected as the next focal point. These steps were repeated until a focal point was reached that had no neighbors (N=Ø), regardless of the distance. The normal angle of a group is defined as the average angle between the directions of any pairs of norms within this group:

$$\alpha_g = \sum_{i,j=1}^{m} \frac{1}{C_m^2} \left\{ \cos^{-1} \left[\frac{\left| (\overrightarrow{sn_i} \times \overrightarrow{sn_{i+1}}) \bullet (\overrightarrow{sn_j} \times \overrightarrow{sn_{j+1}}) \right|}{\left\| \overrightarrow{sn_i} \times \overrightarrow{sn_{i+1}} \right\| \left\| \overrightarrow{sn_j} \times \overrightarrow{sn_{j+1}} \right\|} \right] \right\} \tag{1}$$

where s is the focal point, n_i and n_j are points in this group, m is the number of the points in this group, "|| ||" is the vector length operator, and C_m^2 is the number of possible angles between normal direction. The threshold angle determined the number of reference points and the model's representation of manually defined structures. Larger threshold angles resulted in less reference points and less accuracy, and vice versa. We determined the threshold angle experimentally. The 30 degree was selected in this study because this threshold angle resulted in smaller number of reference points while maintaining acceptable accuracy (kappa index of 0.90 or higher). The simplified reference points were then triangulated by using a process similar to the Voronoi graph method [14].

To evaluate how well the triangular mesh models represented the true structures, we defined the volumes of structures based on mesh models. The similarities between mesh-defined volumes and manually delineated volumes were evaluated by calculation of a kappa index for each individual structure model:

$$\kappa(S_a, S_b) = \frac{2|S_a \cap S_b|}{|S_a| + |S_b|} \tag{2}$$

where S_a refers to the structure defined by the mesh models and S_b refers to the manually delineated structure.

3   Results

Figure 1 clearly demonstrates the dependencies, relationships, and positioning of boundary conditions defined for each of the 25 cortical and subcortical regions. A semi-transparent surface rendering of these manually delineated brain structures is provided in Figure 2. The similarity of intra-rater between two sessions for left frontal lobe was 0.98. These manually delineated structures formed the basis for the individual triangular mesh models. After validation and refinement of these models by the neuroradiologist, we generated the triangular mesh models as shown in Figure 3. We then visually inspected the resulting triangular mesh models to check the validity of node assignment and triangle formation as representative of the true surface, which had been manually delineated.
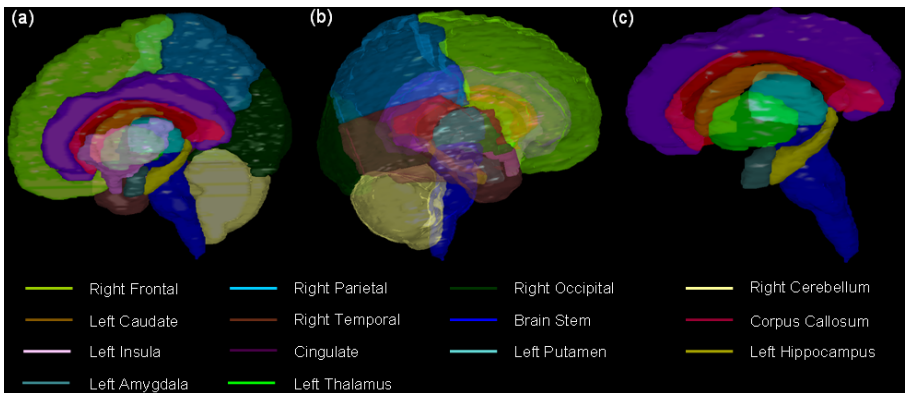

Fig. 2. Semitransparent surface of manually defined brain structures. The structures on either hemisphere were selected for illustration purposes. (a) Right lateral view with all structures. (b) Left lateral view with all structures. (c) Right lateral view with subcortical structures (insula was excluded to make it easier to see the putamen and thalamus).
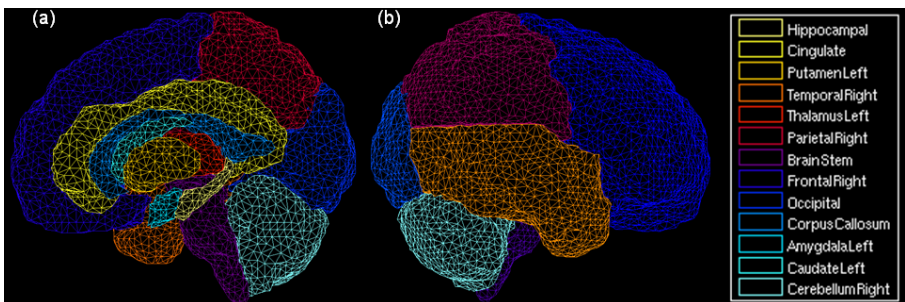

Fig. 3. Triangular mesh models of brain structures. The structures on either hemisphere were selected for the purpose of illustration. (a) Right lateral view with all structures. (b) Left lateral view with all structures.

The similarities between manually defined structures and models were assessed by calculation of the kappa statistic. The average kappa index for cortical structures (frontal lobe, parietal lobe, temporal lobe, occipital lobe, cerebellum, and brain stem) was 0.97, and it ranged from a low of 0.92 in the brain stem to 0.98 or 0.97 in all other cortical regions. The average kappa index for the subcortical structures (amygdale, caudate, hippocampus, thalamus, insula, putamen, cingulate cortex, and corpus callosum) was 0.91, and it ranged from a low of 0.87 in the hippocampus to highs of 0.95 in the thalamus and cingulate cortex.

4   Discussion

We have included WM in lobes during manual tracing of the brain although anatomic textbooks define lobes as gray matter [11]. Our rationale was two-fold. First, if future studies required exclusion of WM in lobes, WM could be automatically removed by tissue segmentation methods. In contrast, manually tracing the WM/GM convolution would have been a tedious procedure and one prone to error. Second, WM is generally associated with specific lobes during the planning of radiation therapy and neuroimaging studies. WM tissue is made up of fibers that convey impulses to and from lobes (projection fibers), between different lobes (association fibers), and within the same lobe in the contralateral hemisphere (commissural fibers). The inclusion of WM in the definition of lobes does not consider the integrity of WM fibers; however, it does provide a rough estimation of WM fibers associated with individual lobes.

We are developing a knowledge-guided active model (KAM) method for cortical structure segmentation on pediatric MR images based on this pediatric brain atlas. Triangular mesh models will be transformed to images of a given subject by maximizing entropy (normalized mutual information), and then actively slithered to the boundaries of structures by minimizing enthalpy. Our experience has suggested that the atlas could be applied for rough cortical structure segmentation by a registration method and more accurate individualized segmentation by an active model method [15].

In summary, we have constructed a digital pediatric brain atlas and its triangular mesh models for 25 cortical and subcortical brain structures, which are publicly available on the Internet (www.stjude.org/brainatlas). The atlas differs from previous brain atlases in that it was developed specifically for young children and in the fact that the WM has been roughly divided into WM associated with a specific lobe, WM that connects different regions, WM that interconnects two hemispheres, and WM that connects all lobes with subcortical structures. The atlas and its mesh models can be used in knowledge-based pediatric brain structure segmentation, shape analysis, and planning treatment.

References

1. Ganser K.A., Dickhaus H., Metzner R., et al: A deformable digital brain atlas system according to Talairach and Tournoux. Medical Image Analysis 8 (2004) 3-22
2. Pommert A., Riemer M., Schiemann T., et al: Knowledge-Based and 3D Imaging-Systems in Medical-Education. Information Processing '94, Vol II IFIP Trans A-Computer Sci. and Tech. 52 (1994) 525-532
3. Kikinis R., Shenton M.E., Iosifescu D.V., et al: A digital brain atlas for surgical planning, model-driven segmentation, and teaching. IEEE Tran. Visualization and Computer Graphics 2 (1996) 232-241
4. Thurfjell L., Bohm C., Bengtsson E.: Cba - An Atlas-Based Software Tool Used to Facilitate the Interpretation of Neuroimaging Data. Computer Methods and Programs in Biomedicine 47 (1995) 51-71
5. Tzourio-Mazoyer N., Landeau B., Papathanassiou D., et al: Automated anatomical labeling of activations in SPM using a macroscopic anatomical parcellation of the MNI MRI single-subject brain. Neuroimage 15 (2002) 273-289
6. Paus T., Zijdenbos A., Worsley K., et al: Structural maturation of neural pathways in children and adolescents: In vivo study. Science 283 (1999) 1908-1911
7. Wilke M., Schmithorst V.J., Holland S.K.: Normative pediatric brain data for spatial normalization and segmentation differs from standard adult data. Magnetic Resonance in Medicine 50 (2003) 749-757
8. Kates W.R., Warsofsky I.S., Patwardhan A., et al: Automated Talairach atlas-based parcellation and measurement of cerebral lobes in children. Psychiatry Research-Neuroimaging 91 (1999) 11-30
9. Maes F., Collignon A., Vandermeulen D., et al: Multimodality image registration by maximization of mutual information. IEEE Trans. Med. Imaging 16 (1997) 187-198
10. Press W.H., Vetterling W.T., Flannery B.P.: Numerical Recipes in C, 2nd Ed. New York CAMBRIDGE UNIVERSITY PRESS (1992)
11. Carpenter M.B.: Core text of neuroanatomy, 3rd Ed. Baltimore, MD Williams & Wilkins (1985)
12. Kim J.J., Crespo-Facorro B., Andreasen N.C., et al: An MRI-based parcellation method for the temporal lobe. Neuroimage 11 (2000) 271-288
13. Crespo-Facorro B., Kim J.J., Andreasen N.C., et al: Human frontal cortex: An MRI-based parcellation method. Neuroimage 10 (1999) 500-519
14. Berg D.M., Kreveld van M., Overmars M., et al: Computational geometry: algorithms and applications, 2nd rev. ed. Berlin, Germany Springer-Verlag (2000)
15. Shan Z.Y., Parra C., Ji Q., Jain J., Reddick W.E. A Knowledge-Guided Active Model Method of Cortical Structure Segmentation on Pediatric MR images. J Magn Reson Imging, In Press.